ACS OMEGA

Nanoscale Mapping of Bromide Segregation on the Cross Sections of Complex Hybrid Perovskite Photovoltaic Films Using Secondary Electron Hyperspectral Imaging in a Scanning Electron Microscope

Vikas Kumar,*,[†] Whitney L. Schmidt,[†] Giorgio Schileo,[†] Robert C. Masters,[†] Michael Wong-Stringer,[‡] Derek C. Sinclair,[†] Ian M. Reaney,[†] David Lidzey,[‡] and Cornelia Rodenburg*,[†]

[†]Department of Materials Science and Engineering, University of Sheffield, Mappin Street, Sheffield S1 3JD, U.K.
[‡]Department of Physics and Astronomy, University of Sheffield, Hounsfield Road, Sheffield S3 7RH, U.K.

S *Supporting Information*

ABSTRACT: Mixed halide (I/Br) complex organic/inorganic hybrid perovskite materials have attracted much attention recently because of their excellent photovoltaic properties. Although it has been proposed that their stability is linked to the chemical inhomogeneity of I/Br, no direct proof has been offered to date. Here, we report a new method, secondary electron hyperspectral imaging (SEHI), which allows direct imaging of the local variation in Br concentration in mixed halide (I/Br) organic/inorganic hybrid perovskites on a nanometric scale. We confirm the presence of a nonuniform Br distribution with variation in concentration within the grain interiors and boundaries and demonstrate how SEHI in conjunction with low-voltage scanning electron microscopy can enhance the understanding of the fundamental physics and materials science of organic/inorganic hybrid photovoltaics, illustrating its potential for research and development in "real-world" applications.
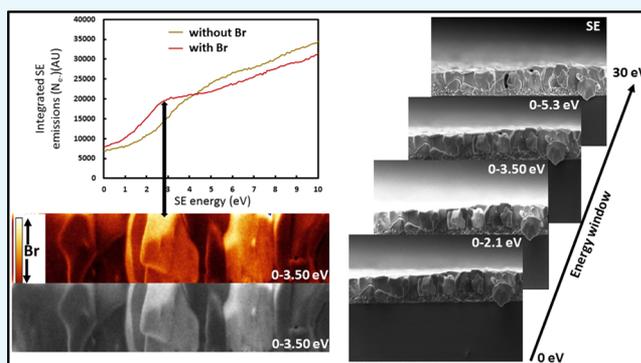
1. INTRODUCTION

Metal halide organic/inorganic perovskite photovoltaic materials that crystallize with an ABX_3 structure have attracted intense academic and industrial attention for optoelectronic applications.[1−4] In this ABX_3 structure, A, B, and X are monovalent cations [methylammonium (MA), formamidinium (FA), and cesium (Cs)], divalent cations (Pb and Sn), and halide anions (I, Cl, and Br), respectively.[5−7] Of the various organic/inorganic perovskite materials, methylammonium lead triiodide (MAPbI$_3$) is the most studied material for photovoltaic devices.[8] However, focus has now shifted towards solid solutions of hybrid perovskite materials with multiple A- and X-site species to enhance stability against ambient moisture[9,10] and to improve the photovoltaic properties.[5,8] As a consequence, the structural, thermal, and photovoltaic properties of mixed I/Br perovskites have been widely investigated.[11,12] Nevertheless, conclusions regarding local halide composition and distribution remain speculative even though they are considered responsible for charge carrier recombination by creating trapped states[13] that collectively affect the optoelectronic performance.[14]

As it has been established that the structure and composition of heavily mixed hybrid perovskites (HPs) is very complex because of the occurrence of spontaneous spinodal decomposition, amorphous impurities, and related nanoscale phase segregation,[15] a novel, fast microscopy technique that can reveal

such variations in films and real devices is urgently called for.[16] This is to enable further advances in the device performance. Therefore, here we introduce a fast hyperspectral imaging technique based on the secondary electron (SE) signal in a low-voltage (LV) scanning electron microscope. Hyperspectral imaging is the integration of conventional imaging and spectroscopy to attain both spatial and spectral information.[17] Because we integrate the SE spectroscopy with SE imaging, we refer to this method as secondary electron hyperspectral imaging (SEHI) in which carefully selected spectral window(s) within the overall SE signal is used to reveal the presence of nanoscale inhomogeneities in Br composition in the lateral direction and across the film thickness with a sub-10 nm resolution. In addition, SEHI enables the observation and identification of nanosized local regions with excess organic material in complex organolead mixed-halide perovskite films that resemble device structures. Thus, we find that SEHI enables direct observation of several nanoscale features in organolead mixed-halide perovskites, which cannot be revealed using conventional scanning electron microscopy (SEM), LV-SEM, or any other analytical technique because of the different
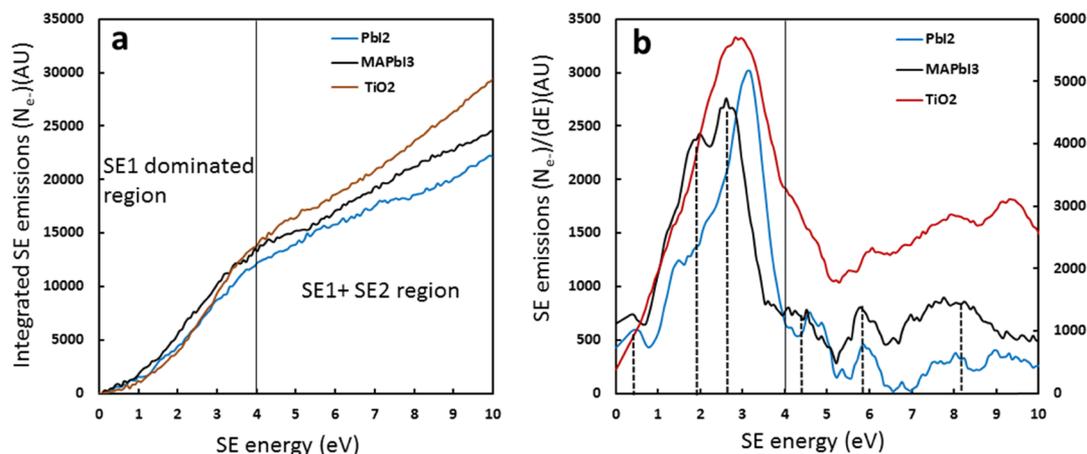
Figure 1. Measured SE spectra: (a) Integrated SE spectra of TiO$_2$, PbI$_2$, and MAPbI$_3$ and (b) differentiated SE spectra of TiO$_2$, PbI$_2$, and MAPbI$_3$.

constrains of many standard analytical techniques, as summarized below.

Currently, energy dispersive X-ray (EDX) spectroscopy is the main analytical tool inside of a scanning electron microscope for elemental mapping;[18,19] however, this technique is limited because of its spatial resolution, which is typically about 1 μm, and is not suitable for materials that require lower electron beam energy ($\leq$1 kV) because there is insufficient energy to excite characteristic X-rays. Even for electron beam energies typically used for EDX, organic/inorganic hybrid perovskite photovoltaic materials, without the application of any top conductive coating, suffer damage during irradiation due to because of a combination of the intensity (typically 86 pA) and kinetic energy (at 10 keV) of the electrons.[20]

Halides are particularly difficult to detect using standard scanning electron microscopy (SEM) imaging techniques, where typically a high-energy electron beam is used as the primary source of excitation, giving rise to excitation of surface atoms, which provides energy for dissociation, desorption, and chemical reactions. The cross section for electron-stimulated dissociation of nominally gaseous species ranges from 10^{-15} cm^2 down to unmeasurably small values,[21] with halides exhibiting the highest values and therefore making these difficult to detect. Nevertheless, a gradient between Br and I concentration over a length of several micrometers can be mapped using SEM-EDX, as recently demonstrated.[22]

Imaging of chemical variations on the submicron scale, without the application of a conductive coating, requires a radically different approach that allows the minimization of both incident beam energy and beam current. This can be realized by exploiting the SE signal. This approach enables imaging with a high resolution and minimum damage in a situation where the atomic number contrast between the mixed components of the perovskite photovoltaic materials is too low in conventional SEM to provide information about the spatial distribution of, for example, the anion species. The overall SE signal consists of contributions from both SE1 and SE2.[23,24] SEs generated directly by the incident primary electrons through inelastic interactions with the electrons of the material to be analyzed are known as SE1 and carry high-resolution, surface-specific information about the electronic structure of the material. SE2 are produced by electrons scattered elastically by the nuclei of the atoms present in the material prior to SE generation. Although the SE2 signal contains average atomic number contrast and is 2−3 times the magnitude of the SE1

signal,[20] it provides a limited resolution in an SE image in conventional SEM. Furthermore, the average atomic number changes only slightly when I is partially replaced by Br (change of <2 for [PbI$_3$]$^-$ and [PbI$_2$Br]$^-$) compared with that on the incorporation of Cs (where the change in the average atomic number is almost 20). Hence, the image contrast in conventional SEM of complex triple-cation organic/inorganic hybrid perovskites[25] is dominated by the average atomic number contrast arising from Cs, thus obscuring Br variations. Here, we demonstrate that SE2 can be suppressed (filtered) to generate an image contrast based on SE1, which may then be used to map changes in the local electronic properties (bandgap) with a high spatial resolution. This can be exploited to map Br distributions because the difference in the bandgap on substituting I with Br is substantial (bandgap of MAPbI$_3$ is 1.7 eV compared with 2.3 eV for MAPbBr$_3$).[26] By contrast, the substitution of Cs for MA and FA ions results in a bandgap change of only 0.02 eV.[27]

Energy filtering is already widely used in transmission electron microscopy (TEM) to enhance chemical contrast and provide direct compositional information, with a lateral resolution of 1−2 nm.[28,29] However, this technique relies on the ability to prepare electron transparent samples that do not sustain damage during irradiation under a high-voltage, intensely focused electron beam. Preparation of TEM samples from organic/inorganic hybrid perovskite materials is difficult, and images within the literature are principally of powders and films at a low resolution with no high-quality chemical analysis at the requisite spatial resolution.[30] Such a limitation, of course, does not apply in cases of nanoparticles without any organic component and does not require an additional sample preparation. In fact, if the nanoparticles are small enough, an indication of atomic columns can be seen in the EDX maps of the nonvolatile components, as was demonstrated on the maps of Cs and Pb taken from the CsPbBr$_3$ nanoparticles.[31]

An alternative is ultraviolet photoelectron spectroscopy (UPS), which provides quantitative information about the valence band region and interfaces, but its spatial resolution is poor because ultraviolet lamps illuminate a large area (1 mm^2).[32,33] Micro-Raman spectroscopy has also been used to probe the Br to I concentration ratio in an organic/inorganic mixed halide photovoltaic material.[34] However, laser-induced degradation cannot be avoided, and its resolution is insufficient to map intragranular variations in the halide concentration. Conductive atomic force microscopy

(cAFM) has also been used to map intragranular open circuit voltage and short circuit current homogeneity in Cl- and I-based perovskites. The observed voltage and current values were nonuniform, and variations were related to the facet-dependent density of the trapped states.[35] Photoluminescence (PL), Kelvin probe force microscopy (KPFM), and HIM-SIMS (helium ion microscope coupled with secondary ion mass spectrometer) are other techniques used to map Cl concentration and hypothesize the presence of Cl on the surface,[36] but they have a limited lateral spatial resolution and cannot assess the distribution as a function of film thickness.[37] Here, we present a solution to address the challenge of characterizing the nonuniform distribution (segregation) of Br in photovoltaic-applicable perovskite materials using SEHI and further demonstrate on fracture surfaces of the photovoltaics film, sub-10 nm resolution and high chemical contrast images, illustrating the Br distribution. However, no Br-related chemical contrast would be expected if Br was distributed uniformly throughout the material.

2. RESULTS AND DISCUSSION

2.1. Origin of SE Peaks in SE Spectra. SEHI has never been used to characterize perovskite solar cell materials and is not well-understood even for much simpler materials such as metals.[38] We first identify the origin of the SE emission spectra, with the aim of mapping halide distributions in mixed cation [Cs and formamidinium iodide (FAI)]-based and halide (I/Br)-based organic/inorganic hybrid perovskites.

Collecting SE spectra of a number of materials used in such devices allows some insight into which particular energy regions are suitable to map chemical distributions while suppressing other types of contrast (e.g., topography). The integrated spectra of TiO_2, PbI_2, and $MAPbI_3$ are shown in Figure 1a. For SEs emitted with energies <4 eV, the integrated SE spectra of all three materials are similar, but substantial differences emerge at energies >4 eV. This effect is also clearly observed when comparing the same compound that differs only in particle size, as illustrated for TiO_2. The particle size was determined using autocorrelation functions as described in Figure S1a,b, and comparisons were made on two different TiO_2 films (1 and 2) where the particle size of the $TiO_2(1)$ film is smaller than that of the $TiO_2(2)$ film (Figure S1a,b). We therefore conclude that structural effects play a role in the emission of SEs with energies exceeding 4 eV, rendering SEs in this energy range unreliable for chemical mapping. By contrast, the emission of SEs with energies <4 eV is not affected by the particle size and, importantly, differences in the volume fraction do not seem to have a strong influence on the spectrum. We conclude that SEs at energies <4 eV (are largely SE1[23,24]) result from a direct interaction of the primary electron with the material and may reflect aspects of the electronic band structure. For less complex materials such as highly oriented pyrolytic graphite (HOPG), a close link with the UPS spectra was determined,[39] and we propose that this may also be the case for $MAPbI_3$. To test this hypothesis, Figure 1b shows the first derivative of the data presented in Figure 1a. We note the presence of a fine structure in the spectra of both PbI_2 and $MAPbI_3$, with all peak positions listed in Table 1. The observed peak positions for $MAPbI_3$ in Figure 1b are in good agreement with those found in the valence band spectra of $MAPbI_3$ measured using UPS.[28] The positions of these peaks are indicated in Figure 1b by the dashed vertical lines. A direct comparison of the UPS and SE spectra is presented in Figure S2. We thus conclude that SEs

**Table 1. Summary of Differentiated Curve Peak Positions of PbI_2, $MAPbI_3$, and TiO_2 from Figure 1b[a]**

material	peaks position (eV)					
PbI_2	0.45	1.5	3.15	4.6	5.85	7.8
$MAPbI_3$	0.35 (0.45)	1.9 (1.9)	2.6 (2.6)	4.6 (4.25)	5.85 (5.80)	8.0 (8.20)
TiO_2	2.8	5.9	7.9	9.4		

[a]Values in brackets are the corresponding UPS peaks for $MAPbI_3$.[33]

with energies <4 eV may be used for mapping chemical variations based on changes in the band structure, and SEHI may be used to select the most suitable energy window for a specific material.

2.2. Contrast for Organic/Inorganic Hybrid Perovskite Materials with Multiple A- and X-Species. Figure 2a shows the integrated SE spectra of HP1 and HP2 where the lower-energy region of SE spectra are similar, confirming that the Cs concentration variation does not affect the SE emission in the low-energy range and hence does not drastically alter the band structure. It would therefore be difficult to identify the Cs distribution in the SEHI cross-sectional images in this low-energy region. Our greatest interest, however, is the mapping of Br because of its expected influence on device stability and photovoltaic properties. The SE spectra of Br-doped hybrid perovskite HP3 are plotted in Figure 2b. The low-energy region (<4 eV) of the SE emission is strongly increased compared with non-Br-containing perovskites (HP2), and thus, Br-rich regions appear bright in SEHI images taken with an energy window of 0–3.5 eV. To predict the window of maximum Br contrast and to check that the contrast does indeed originate from Br variations, we plotted the predicted contrast curve in Figure 2c. These contrast curves were derived from the SE spectra in Figure 2b using eq 1 (see Materials and Methods). We observe a high contrast energy window of 0–4 eV for HP3/HP2, with peaks in contrast of ~20.0% at 2.4 eV which is related to the inclusion of Br (see Table 2), whereas the change in the Cs composition is reflected in the contrast plot for HP2/HP1, yielding no more than 6% contrast at its peak. Hence, the dominant contrast relates to the presence of Br when imaging is carried out at the 0–4 eV energy window. To verify that the bright contrast is indeed caused by Br and not Cs, we present images taken from smaller energy windows 2.1–3.5 and 3.5–5.3 eV. The contrast curve in Figure 2c predicts positive contrast for both Br- and Cs-rich regions in images taken with the 2.1–3.5 eV window. However, the prediction for images taken in the 3.5–5.3 eV window is that there is no Cs-related contrast and a clear contrast reversal is due to Br (e.g., the highest Br concentration will appear the darkest). The latter is indeed observed (see Figure S4b) and is further evidence that the contrast stems from Br segregation. Furthermore, we investigate the contrast in a specimen with 100% Br (no Cs or I) and check for Br segregation-related contrast with the same method as above (see Figure S4c), in which case we do not observe any Br segregation but indications of access organic material. This demonstrates the power of hyperspectral imaging, where multiple images of the same area taken with different SE energy windows can be used to identify the cause of contrast.

The differentiated SE spectra of HP1, HP2, and HP3 perovskite materials are shown in Figure 2d. The peak positions for both HP1 and HP2 in the low-energy region are at 0.5, 1.3, 2.2, and 3.0 eV and are consistent, albeit having slightly
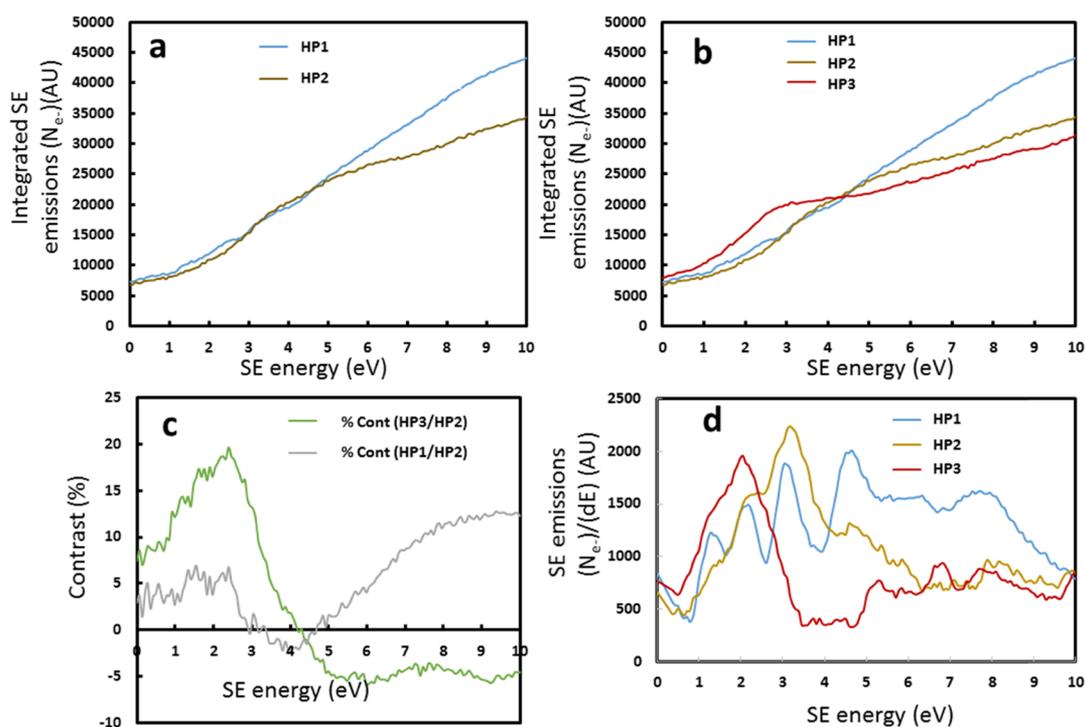
Figure 2. Measured SE spectra of the HP1, HP2, and HP3 perovskite materials. (a) Integrated SE spectra of HP1 and HP2, (b) integrated SE spectra of HP1, HP2, and HP3, (c) predicted contrast plots [calculated from the data in 2b using the SE contrast equation (see Materials and Methods)], and (d) differentiated SE spectra of HP1, HP2, and HP3.

Table 2. Chemical Compositions of Different Perovskite Systems (Named HP1, HP2, and HP3) with $0.05 < x < 0.3$ and $0.2 < y < 1.0$

sample name	chemical composition
HP1	$Cs_{0.50}FAI_{0.50}PbI_3$
HP2	$Cs_xFAI_{1-x}PbI_3$
HP3	$Cs_xFAI_{1-x}PbI_{3-y}Br_y$

different peak intensities. The change in the SE intensity may be due to small variations in the bandgap for the different compositions. For example, the 1.3 eV peak for HP2 is not well-pronounced; however, it has an enhanced intensity for HP1. Most notable, however, is the change in the peak width. The peaks in the SE spectra of the material with a higher organic content (HP2) are less sharp than those in HP1 (Figure 2d), indicating that the Cs-doped perovskite system may have a more ordered electronic structure, in accordance with refs 40 and 41.

Indeed, it was previously reported that an increase in the Cs content led to the formation of a sharp absorption onset in $FA_{(1-x)}Cs_xPb(I_{0.6}Br_{0.4})_3$ materials, which was taken as an indication of a more ordered crystalline perovskite material with an increased Cs content.[42] This further points to the similarities in the characteristics of the SE spectra and optical absorption spectra because both are influenced by the crystalline order of the material. Because the optical bandgap is derived from the onset of the optical absorption spectra, a strong effect of bandgap on the onset, and hence the low-energy region of the SE spectra, is to be expected. Given the well-established change in the electronic band structure as a result of partially replacing I with Br,[43−45] it is not surprising that the addition of Br in the HP3 perovskite has a pronounced effect on the shape of the SE spectrum in the low-energy

region. The most intense peak in the spectrum of HP3 is observed at 2.1 eV, whereas for HP2, it is at 3.2 eV. From these results, we conclude that the HP2/HP1 contrast curve (Figure 2c) lends itself to hyperspectral imaging of the distribution of Br, which is the focus of the next section.

2.3. Nanoscale Mapping of Br in Organic/Inorganic Hybrid Perovskites. The variation of Br with depth has been previously postulated.[12,46] HIM-SIMS has been reported to be capable of mapping Br with a nanoscale resolution, but it has not been attempted to date;[37] however, lateral profiling with HIM-SIMS has revealed significant variation in the lateral Br concentration over 300 nm range. Here, we demonstrate that hyperspectral imaging is an ideal technique for Br mapping. As shown in Figure 3, we compare standard SE and hyperspectral cross-sectional images (in the energy range of 0−3.5 eV) of HP3 perovskite materials where the grain size is 300−500 nm. Figure 3a,b displays standard SE images without (Figure 3a) and with sample tilt (Figure 3b). Figure 3c,d shows the corresponding hyperspectral images of the HP3 perovskite (in the energy range of 0−3.50 eV). We first compare the contrast in the case of normal electron beam incidence (no sample tilt). In the standard SE image (Figure 3a), the contrast is almost uniform throughout the cross section, whereas in the corresponding hyperspectral images (Figure 3c), a clear contrast variation between the neighboring grains is observed (Figure S3). Because of the choice of the energy window (see Figure 2b,d), we can expect brighter grains in Figure 3c to contain an increased concentration of Br with respect to other regions and also expect the magnitude of the Br-related contrast to depend on the position and width of the energy window used to form the image. That this is indeed the case is shown in Figure S4a,b; hence, the strong contrast between the grains in Figure 3c is due to the presence of an inhomogeneous distribution of Br. The contrast principally arises from the
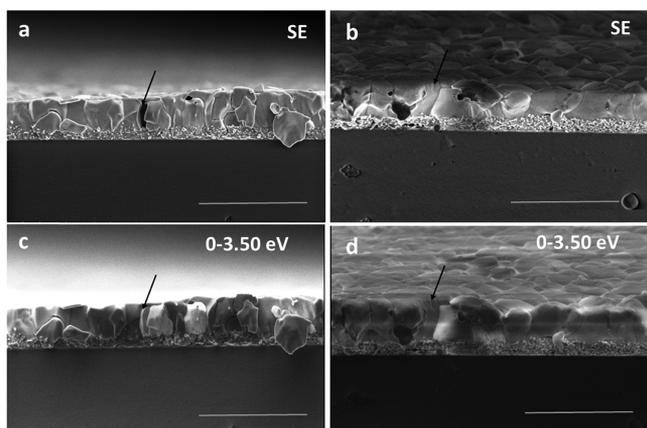
Figure 3. Standard SE and hyperspectral cross-sectional images of the HP3 perovskite: (a) Standard SE image, (b) tilted standard SE image, (c) hyperspectral image at 0−3.5 eV, and (d) tilted hyperspectral image at 0−3.5 eV. The scale bars represent 2 μm.

difference in the band structure between Br- and I-based perovskites. The high contrast difference (∼75.0%) between Br-rich and I-rich grains in Figure 3c is consistent with that observed as a result of band-off sets in doped regions in semiconductors and for molecules that are highly diluted within a host self-assembled monolayer.[47−49] The Br concentration variations can be mapped with a sub-10 nm resolution as determined from the line profile across two grains, one of which is Br-rich (see Figure S5).

The contrast due to variations in the electronic structure also leads to other notable differences between the standard SE image (Figure 3a) and the hyperspectral image (Figure 3c). In the standard SE image, an area (indicated by the black arrow) in Figure 3a with weak SE emission that appears black can be observed and is likely to be interpreted as a void. The same area in the hyperspectral image contradicts such a conclusion and identifies this as an area containing excess organic material. In the standard SE image, the contrast on a flat surface is dominated by differences in the atomic number (due to the substantial proportion of SE2). We confirm this further by the images shown in Figure S6, in which the stoichiometry of the perovskite was varied. Here, changes in the organic content (MAI) can lead to up to 45% contrast variations in the standard SE image, while being suppressed in the SEHI. For images formed from low-energy SEs only, the atomic number contrast is suppressed and the main contrast mechanism is due to differences in the electronic band structure.

The above conclusions still hold when the sample is tilted, as shown in Figure 3b,d, which permits inspection of the fracture surface and allows more accurate determination of the Br distribution, more specifically whether Br resides at the grain interior or boundary. We conclude that the fracture propagation is largely intergranular with occasional trans-granular regions (we refer the reader to Figures S7 and S8 for detailed evidence toward this conclusion). The contrast in the tilted hyperspectral image (Figure 3d) differs between the two neighboring grains at the grain boundary (indicated by an arrow) and also within the grain on the right of the grain boundary. Part of the right grain appears bright, and hence, we conclude that it is Br-rich but that the Br concentration decreases (becomes darker across the grain). The grain to the left of the boundary remains dark and thus is not Br-rich.

From Figure 3c,d it can be observed that these bright Br-rich areas are not continuous throughout the perovskite layer and instead are capped by dark grains (see Figure S9). This illustrates the value of studying cross sections rather than top surfaces only that are insensitive to through-thickness variations in the composition (see Figure S10).

Regions of intergranular fracture permit the investigation of Br distribution along the grain boundaries. Figure 4 shows the
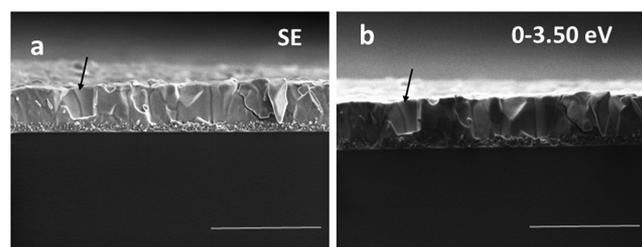
Figure 4. Standard SE and hyperspectral cross-sectional images of the HP3 perovskite: (a) Standard SE image and (b) hyperspectral image at 0−3.5 eV. The scale bars represent 2 μm.

images of an area in which the fracture process resulted in the loss of a grain (indicated by the black arrow), as can be seen by the uneven fracture front and cavity formation evident in both the standard SE image (Figure 4a) and the hyperspectral image (Figure 4b) (see Figure S11, which shows Br-rich cavities left behind). We now compare the contrast between the remaining cavity walls in Figure 4a,b. In the hyperspectral image (Figure 4b), the cavity walls are significantly brighter compared with the surface of the neighboring grain, whereas in the standard SE image (Figure 4a), the contrast is almost uniform. We therefore conclude that the cavity walls and hence these particular grain boundaries are Br-rich, but we do not find evidence that this is the case for all grain boundaries. Our experimental results indicate that the Br distribution is not solely limited to grain boundaries but also varies between and within grains. Furthermore, the probability of finding Br-rich grains on the surface is low because of the presence of capping grains, as indicated in Figure 3c. These grains are thin (20−40 nm) but easily visible within the hyperspectral images. The capping layer is specific to this material system, but the nonuniform Br distribution can also be seen in other Br-based perovskite systems, for example, $MA_{(1−x)}FA_{(x)}PbI_{(3−y)}Br_{(y)}$ (see Figure S12).

Local variations in the Br concentration in the organic/inorganic hybrid perovskites are thus clearly demonstrated using hyperspectral imaging, and we postulate that these have not previously been observed using techniques such as SIMS depth profiling because of limitations to their lateral and vertical nanometer-scale resolutions.[37] Furthermore, because of the excellent sub-10 nm spatial resolution used here, we demonstrate direct evidence that some of the Br is concentrated at the grain boundaries in a manner similar to that reported for Cl.[46] Because local inhomogeneities in the Br concentration have been identified as crucial for further progress of the field,[12,37,46] we expect our method to make a significant contribution to this area.

3. CONCLUSIONS

In conclusion, we present a rigorous validation process for the origin of image contrast in hyperspectral SE imaging, which is not limited to organic/inorganic hybrid perovskites. More

generally, we conclude that the separation of SE1 from the SE2 signal will be possible using hyperspectral imaging. This facilitates investigation of a material in terms of density-related changes and electronic properties, which is of great interest in, for example, two-dimensional materials or nanostructured natural materials (e.g., silk).[50−52]

4. MATERIALS AND METHODS

4.1. Materials. SE spectra were collected for methylammonium iodide (MAI)-, methylammonium bromide (MABr)-, cesium (Cs)-, and FAI-based hybrid perovskites. The structures investigated were based on glass/FTO/m-TiO$_2$/CH$_3$NH$_3$PbI$_3$ for MAPbI$_3$-based samples and glass/FTO/m-TiO$_2$/ Cs$_{(1−x)}$FA$_{(x)}$PbI$_{(3−y)}$Br$_y$ (where $0.05 < x < 0.3$ and $0.2 < y < 1.0$) for Cs/FA mixed halide-based perovskite samples (supplied by Dyesol UK Ltd.). For MA/FA and mixed halide-based perovskite samples (supplied by Michael Stringer), the structure was glass/FTO/c-TiO$_2$/m-TiO$_2$/ MA$_{(1−x)}$FA$_{(x)}$PbI$_{(3−y)}$Br$_{(y)}$ (where $0.05 < x < 0.15$ and $0.05 < y < 0.15$).

4.2. Hyperspectral Imaging. The basic principles of the experimental method to collect SE spectra have been reported elsewhere.[53] In this work, we used an FEI Nova NanoSEM 450 scanning electron microscope. All samples were imaged using a through-lens detector (TLD) at a working distance of 2 mm with a beam current of 16 pA and an accelerating voltage of 1 kV. Hyperspectral imaging window selection was performed by varying the bias to the deflector electrode, and a sequence of SE images was taken by increasing the deflector voltage (0−10 eV), with a step size of 0.2 eV. The dwell time was adjusted to 200 ns. We measured and compared the SE spectra of individual layers and their stack to identify the spectral window for individual materials. We plotted SE emission with reference to the applied deflector voltage for individual materials and calculated the hyperspectral energy window using the Seiler SE contrast equation. The contrast (C) is given by eq 1[23]

$$C = \frac{I_1 - I_2}{I_1 + I_2} \cdot 100\% \tag{1}$$

where I_1 and I_2 represent the SE emission intensity of individual materials. Complete structures were then imaged using these energy windows.

ASSOCIATED CONTENT

Supporting Information

The Supporting Information is available free of charge on the ACS Publications website at DOI: 10.1021/acsomega.7b00265.

Additional secondary electron spectra, hyperspectral images, and lateral resolution profiles curve; further evidence of average atomic number contrast and electronic contrast in hyperspectral images and the evidence of role of surface topography; and further evidence of bromide inhomogeneity in different perovskite material systems (PDF)

AUTHOR INFORMATION

Corresponding Authors
*E-mail: vikas.kumar@sheffield.ac.uk (V.K.).
*E-mail: c.rodenburg@sheffield.ac.uk (C.R.).

ORCID
Vikas Kumar: 0000-0002-1034-2915
Michael Wong-Stringer: 0000-0002-4364-4127
Derek C. Sinclair: 0000-0002-8031-7678
Ian M. Reaney: 0000-0003-3893-6544

Notes
The authors declare no competing financial interest.
Full datasets of all the spectra can be found at https://figshare.com/s/a9bd40f7a7eae2dadd20.

REFERENCES

(1) Green, M. A.; Ho-Baillie, A.; Snaith, H. J. The emergence of perovskite solar cells. *Nat. Photonics* **2014**, *8*, 506−514.

(2) Bai, Y.; Dong, Q.; Shao, Y.; Deng, Y.; Wang, Q.; Shen, L.; Wang, D.; Wei, W.; Huang, J. Enhancing stability and efficiency of perovskite solar cells with crosslinkable silane-functionalized and doped fullerene. *Nat. Commun.* **2016**, *7*, 12806.

(3) Tan, Z.-K.; Moghaddam, R. S.; Lai, M. L.; Docampo, P.; Higler, R.; Deschler, F.; Price, M.; Sadhanala, A.; Pazos, L. M.; Credgington, D.; Hanusch, F.; Bein, T.; Snaith, H. J.; Friend, R. H. Bright light-emitting diodes based on organometal halide perovskite. *Nat. Nanotechnol.* **2014**, *9*, 687−692.

(4) Stranks, S. D.; Snaith, H. J. Metal-halide perovskites for photovoltaic and light-emitting devices. *Nat. Nanotechnol.* **2015**, *10*, 391−402.

(5) Jeon, N. J.; Noh, J. H.; Yang, W. S.; Kim, Y. C.; Ryu, S.; Seo, J.; Seok, S. I. Compositional engineering of perovskite materials for high-performance solar cells. *Nature* **2015**, *517*, 476−480.

(6) Saliba, M.; Matsui, T.; Seo, J.-Y.; Domanski, K.; Correa-Baena, J.-P.; Nazeeruddin, M. K.; Zakeeruddin, S. M.; Tress, W.; Abate, A.; Hagfeldt, A.; Grätzel, M. Cesium-containing triple cation perovskite solar cells: improved stability, reproducibility and high efficiency. *Energy Environ. Sci.* **2016**, *9*, 1989−1997.

(7) Serrano-Lujan, L.; Espinosa, N.; Larsen-Olsen, T. T.; Abad, J.; Urbina, A.; Krebs, F. C. Tin- and Lead-Based Perovskite Solar Cells under Scrutiny: An Environmental Perspective. *Adv. Energy Mater.* **2015**, *5*, 1501119.

(8) Park, N.-G. Methodologies for high efficiency perovskite solar cells. *Nano Convergence* **2016**, *3*, 1−13.

(9) Deretzis, I.; Alberti, A.; Pellegrino, G.; Smecca, E.; Giannazzo, F.; Sakai, N.; Miyasaka, T.; La Magna, A. Atomistic origins of CH$_3$NH$_3$PbI$_3$ degradation to PbI$_2$ in vacuum. *Appl. Phys. Lett.* **2015**, *106*, 131904.

(10) Yang, J.; Siempelkamp, B. D.; Liu, D.; Kelly, T. L. Investigation of CH$_3$NH$_3$PbI$_3$ Degradation Rates and Mechanisms in Controlled Humidity Environments Using in Situ Techniques. *ACS Nano* **2015**, *9*, 1955−1963.

(11) Jeon, N. J.; Noh, J. H.; Kim, Y. C.; Yang, W. S.; Ryu, S.; Seok, S. I. Solvent engineering for high-performance inorganic−organic hybrid perovskite solar cells. *Nat. Mater.* **2014**, *13*, 897.

(12) Slotcavage, D. J.; Karunadasa, H. I.; McGehee, M. D. Light-Induced Phase Segregation in Halide-Perovskite Absorbers. *ACS Energy Lett.* **2016**, *1*, 1199−1205.

(13) deQuilettes, D. W.; Zhang, W.; Burlakov, V. M.; Graham, D. J.; Leijtens, T.; Osherov, A.; Bulovic, V.; Snaith, H. J.; Ginger, D. S.; Stranks, S. D. Photo-induced halide redistribution in organic−inorganic perovskite films. *Nat. Commun.* **2016**, *7*, 11683.

(14) MacDonald, G. A.; Yang, M.; Berweger, S.; Killgore, J. P.; Kabos, P.; Berry, J. J.; Zhu, K.; DelRio, F. W. Methylammonium lead iodide

grain boundaries exhibit depth-dependent electrical properties. *Energy Environ. Sci.* **2016**, *9*, 3642−3649.

(15) Rosales, B. A.; Men, L.; Cady, S. D.; Hanrahan, M. P.; Rossini, A. J.; Vela, J. Persistent dopants and phase segregation in organolead mixed-halide perovskites. *Chem. Mater.* **2016**, *28*, 6848−6859.

(16) Rosales, B. A.; Hanrahan, M. P.; Boote, B. W.; Rossini, A. J.; Smith, E. A.; Vela, J. Lead halide perovskites: Challenges and opportunities in advanced synthesis and spectroscopy. *ACS Energy Lett.* **2017**, *2*, 906−914.

(17) Gowen, A. A.; O'Donnell, C. P.; Cullen, P. J.; Downey, G.; Frias, J. M. Hyperspectral imaging—an emerging process analytical tool for food quality and safety control. *Trends Food Sci. Technol.* **2007**, *18*, 590−598.

(18) Matteocci, F.; Busby, Y.; Pireaux, J.-J.; Divitini, G.; Cacovich, S.; Ducati, C.; Carlo, A. D. Interface and Composition Analysis on Perovskite Solar Cells. *ACS Appl. Mater. Interfaces* **2015**, *7*, 26176−26183.

(19) Divitini, G.; Cacovich, S.; Matteocci, F.; Cinà, L.; Di Carlo, A.; Ducati, C. In situ observation of heat-induced degradation of perovskite solar cells. *Nat. Energy* **2016**, *1*, 15012.

(20) Yuan, H.; Debroye, E.; Janssen, K.; Naiki, H.; Steuwe, C.; Lu, G.; Moris, M.; Orgiu, E.; Uji-i, H.; De Schryver, F.; Samorì, P.; Hofkens, J.; Roeffaers, M. J. Degradation of Methylammonium Lead Iodide Perovskite Structures through Light and Electron Beam Driven Ion Migration. *J. Phys. Chem. Lett.* **2016**, *7*, 561−566.

(21) Ibach, H. *Electron Spectroscopy for Surface Analysis*; Springer-Verlag Berlin Heidelberg: New York, 1977; pp 3−4.

(22) Tian, W.; Leng, J.; Zhao, C.; Jin, S. Long-Distance Charge Carrier Funneling in Perovskite Nanowires Enabled by Built-in Halide Gradient. *J. Am. Chem. Soc.* **2017**, *139*, 579−582.

(23) Seiler, H. Secondary electron emission in the scanning electron microscope. *J. Appl. Phys.* **1983**, *54*, R1−R18.

(24) Cazaux, J. About the role of the various types of secondary electrons (SE1; SE2; SE3) on the performance of LVSEM. *J. Microsc.* **2004**, *214*, 341−347.

(25) Zhang, M.; Yun, J. S.; Ma, Q.; Zheng, J.; Lau, C. F. J.; Deng, X.; Kim, J.; Kim, D.; Seidel, J.; Green, M. A.; Huang, S.; Ho-Baillie, A. W. Y. High-Efficiency Rubidium-Incorporated Perovskite Solar Cells by Gas Quenching. *ACS Energy Lett.* **2017**, *2*, 438−444.

(26) Schulz, P.; Edri, E.; Kirmayer, S.; Hodes, G.; Cahen, D.; Kahn, A. Interface energetics in organo-metal halide perovskite-based photovoltaic cells. *Energy Environ. Sci.* **2014**, *7*, 1377−1381.

(27) Lee, J.-W.; Kim, D.-H.; Kim, H.-S.; Seo, S.-W.; Cho, S. M.; Park, N.-G. Formamidinium and Cesium Hybridization for Photo- and Moisture-Stable Perovskite Solar Cell. *Adv. Energy Mater.* **2015**, *5*, 1501310.

(28) Wang, S.; Sina, M.; Parikh, P.; Uekert, T.; Shahbazian, B.; Devaraj, A.; Meng, Y. S. Role of 4-*tert*-Butylpyridine as a Hole Transport Layer Morphological Controller in Perovskite Solar Cells. *Nano Lett.* **2016**, *16*, 5594−5600.

(29) Pfannmöller, M.; Flügge, H.; Benner, G.; Wacker, I.; Sommer, C.; Hanselmann, M.; Schmale, S.; Schmidt, H.; Hamprecht, F. A.; Rabe, T.; Kowalsky, W.; Schröder, R. R. Visualizing a Homogeneous Blend in Bulk Heterojunction Polymer Solar Cells by Analytical Electron Microscopy. *Nano Lett.* **2011**, *11*, 3099−3107.

(30) Nanova, D.; Kast, A. K.; Pfannmöller, M.; Müller, C.; Veith, L.; Wacker, I.; Agari, M.; Hermes, W.; Erk, P.; Kowalsky, W.; Schröder, R. R.; Lovrinčić, R. Unraveling the Nanoscale Morphologies of Mesoporous Perovskite Solar Cells and Their Correlation to Device Performance. *Nano Lett.* **2014**, *14*, 2735−2740.

(31) Tong, Y.; Bladt, E.; Aygüler, M. F.; Manzi, A.; Milowska, K. Z.; Hintermayr, V. A.; Docampo, P.; Bals, S.; Urban, A. S.; Polavarapu, L.; Feldmann, J. Highly Luminescent Cesium Lead Halide Perovskite Nanocrystals with Tunable Composition and Thickness by Ultrasonication. *Angew. Chem., Int. Ed.* **2016**, *55*, 13887−13892.

(32) Emara, J.; Schnier, T.; Pourdavoud, N.; Riedl, T.; Meerholz, K.; Olthof, S. Impact of Film Stoichiometry on the Ionization Energy and Electronic Structure of $CH_3NH_3PbI_3$ Perovskites. *Adv. Mater.* **2016**, *28*, 553−559.

(33) Schulz, P.; Whittaker-Brooks, L. L.; MacLeod, B. A.; Olson, D. C.; Loo, Y.-L.; Kahn, A. Electronic Level Alignment in Inverted Organometal Perovskite Solar Cells. *Adv. Mater. Interfaces* **2015**, *2*, 1400532.

(34) Ledinsky, M.; Löper, P.; Niesen, B.; Holovský, J.; Moon, S.-J.; Yum, J.-H.; De Wolf, S.; Fejfar, A.; Ballif, C. Raman Spectroscopy of Organic−Inorganic Halide Perovskites. *J. Phys. Chem. Lett.* **2015**, *6*, 401−406.

(35) Leblebici, S. Y.; Leppert, L.; Li, Y.; Reyes-Lillo, S. E.; Wickenburg, S.; Wong, E.; Lee, J.; Melli, M.; Ziegler, D.; Angell, D. K.; Ogletree, D. F.; Ashby, P. D.; Toma, F. M.; Neaton, J. B.; Sharp, I. D.; Weber-Bargioni, A. Facet-dependent photovoltaic efficiency variations in single grains of hybrid halide perovskite. *Nat. Energy* **2016**, *1*, 16093.

(36) de Quilettes, D. W.; Vorpahl, S. M.; Stranks, S. D.; Nagaoka, H.; Eperon, G. E.; Ziffer, M. E.; Snaith, H. J.; Ginger, D. S. Impact of microstructure on local carrier lifetime in perovskite solar cells. *Science* **2015**, *348*, 683−686.

(37) Gratia, P.; Grancini, G.; Audinot, J.-N.; Jeanbourquin, X.; Mosconi, E.; Zimmermann, I.; Dowsett, D.; Lee, Y.; Grätzel, M.; De Angelis, F.; Sivula, K.; Wirtz, T.; Nazeeruddin, M. K. Intrinsic Halide Segregation at Nanometer Scale Determines the High Efficiency of Mixed Cation/Mixed Halide Perovskite Solar Cells. *J. Am. Chem. Soc.* **2016**, *138*, 15821−15824.

(38) Joy, D. C.; Prasad, M. S.; Meyer, H. M. Experimental secondary electron spectra under SEM conditions. *J. Microsc.* **2004**, *215*, 77−85.

(39) Ferrón, J.; Vidal, R. A.; Bajales, N.; Cristina, L.; Baragiola, R. A. Role of HOPG density of empty electronic states above vacuum on electron emission spectra induced by ions and UV photons. *Surf. Sci.* **2014**, *622*, 83−86.

(40) Hoffman, A.; Brener, R. Origin of the extended fine structure in the secondary-electron-emission spectrum of graphite. *Phys. Rev. B: Condens. Matter Mater. Phys.* **1995**, *51*, 1817−1822.

(41) Hoffman, A. Fine structure in the secondary electron emission spectrum as a spectroscopic tool for carbon surface characterization. *Diamond Relat. Mater.* **1994**, *3*, 691−695.

(42) McMeekin, D. P.; Sadoughi, G.; Rehman, W.; Eperon, G. E.; Saliba, M.; Hörantner, M. T.; Haghighirad, A.; Sakai, N.; Korte, L.; Rech, B.; et al. A mixed-cation lead mixed-halide perovskite absorber for tandem solar cells. *Science* **2016**, *351*, 151−155.

(43) Tombe, S.; Adam, G.; Heilbrunner, H.; Apaydin, D. H.; Ulbricht, C.; Sariciftci, N. S.; Arendse, C. J.; Iwuoha, E.; Scharber, M. C. Optical and electronic properties of mixed halide (X = I, Cl, Br) methylammonium lead perovskite solar cells. *J. Mater. Chem. C* **2017**, *5*, 1714−1723.

(44) Noh, J. H.; Im, S. H.; Heo, J. H.; Mandal, T. N.; Seok, S. I. Chemical Management for Colorful, Efficient, and Stable Inorganic−Organic Hybrid Nanostructured Solar Cells. *Nano Lett.* **2013**, *13*, 1764−1769.

(45) Eperon, G. E.; Stranks, S. D.; Menelaou, C.; Johnston, M. B.; Herz, L. M.; Snaith, H. J. Formamidinium lead trihalide: a broadly tunable perovskite for efficient planar heterojunction solar cells. *Energy Environ. Sci.* **2014**, *7*, 982−988.

(46) Long, R.; Prezhdo, O. V. Dopants Control Electron−Hole Recombination at Perovskite−TiO_2 Interfaces: Ab Initio Time-Domain Study. *ACS Nano* **2015**, *9*, 11143.

(47) Kazemian, P.; Mentink, S. A. M.; Rodenburg, C.; Humphreys, C. J. High resolution quantitative two-dimensional dopant mapping using energy-filtered secondary electron imaging. *J. Appl. Phys.* **2006**, *100*, 054901.

(48) Masters, R. C.; Pearson, A. J.; Glen, T. S.; Sasam, F.-C.; Li, L.; Dapor, M.; Donald, A. M.; Lidzey, D. G.; Rodenburg, C. Sub-nanometre resolution imaging of polymer−fullerene photovoltaic blends using energy-filtered scanning electron microscopy. *Nat. Commun.* **2015**, *6*, 6928.

(49) Srinivasan, C.; Mullen, T. J.; Hohman, J. N.; Anderson, M. E.; Dameron, A. A.; Andrews, A. M.; Dickey, E. C.; Horn, M. W.; Weiss, P. S. Scanning Electron Microscopy of Nanoscale Chemical Patterns. *ACS Nano* **2007**, *1*, 191−201.

(50) Bernardi, M.; Ataca, C.; Palummo, M.; Grossman, J. C. Optical and Electronic Properties of Two-Dimensional Layered Materials. *Nanophotonics* **2017**, *6*, 111−125.

(51) Xu, Z.-Q.; Zhang, Y.; Lin, S.; Zheng, C.; Zhong, Y. L.; Xia, X.; Li, Z.; Sophia, P. J.; Fuhrer, M. S.; Cheng, Y.-B.; Bao, Q. Synthesis and Transfer of Large-Area Monolayer WS_2 Crystals: Moving Toward the Recyclable Use of Sapphire Substrates. *ACS Nano* **2015**, *9*, 6178−6187.

(52) Schneider, D.; Gomopoulos, N.; Koh, C. Y.; Papadopoulos, P.; Kremer, F.; Thomas, E. L.; Fytas, G. Nonlinear control of high-frequency phonons in spider silk. *Nat. Mater.* **2016**, *15*, 1079−1083.

(53) Kazemian, P.; Mentink, S. A. M.; Rodenburg, C.; Humphreys, C. J. Quantitative secondary electron energy filtering in a scanning electron microscope and its applications. *Ultramicroscopy* **2007**, *107*, 140−150.